ARTICLE

Check for updates

An Air-Rechargeable Zn Battery Enabled by Organic–Inorganic Hybrid Cathode

Junjie Shi[1], Ke Mao[1,2], Qixiang Zhang[1], Zunyu Liu[1], Fei Long[1,2], Li Wen[1], Yixin Hou[1], Xinliang Li[3], Yanan Ma[4], Yang Yue[1,5] ✉, Luying Li[1], Chunyi Zhi[3], Yihua Gao[1,4] ✉

HIGHLIGHTS

- The excellent performance of MoS_2/PANI cathode is due to better conductivity and desolvation shielding.

- The self-charging zinc battery was successfully assembled that achieve deep self-discharge and long cycle life.

- The quasi solid state battery and battery module have excellent performance and practicability.

ABSTRACT Self-charging power systems collecting energy harvesting technology and batteries are attracting extensive attention. To solve the disadvantages of the traditional integrated system, such as highly dependent on energy supply and complex structure, an air-rechargeable Zn battery based on MoS_2/PANI cathode is reported. Benefited from the excellent conductivity desolvation shield of PANI, the MoS_2/PANI cathode exhibits ultra-high capacity (304.98 mAh g^{-1} in N_2 and 351.25 mAh g^{-1} in air). In particular, this battery has the ability to collect, convert and store energy simultaneously by an air-rechargeable process of the spontaneous redox reaction between the discharged cathode and O_2 from air. The air-rechargeable Zn batteries

display a high open-circuit voltage (1.15 V), an unforgettable discharge capacity (316.09 mAh g^{-1} and the air-rechargeable depth is 89.99%) and good air-recharging stability (291.22 mAh g^{-1} after 50 air recharging/galvanostatic current discharge cycle). Most importantly, both our quasi-solid zinc ion batteries and batteries modules have excellent performance and practicability. This work will provide a promising research direction for the material design and device assembly of the next-generation self-powered system.
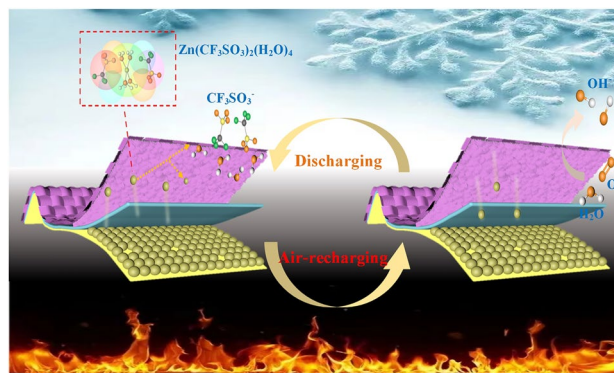
KEYWORDS Air-rechargeable; MoS_2/PANI Cathode; Desolvation shield; Energy storage mechanism; Zn batteries module

Junjie Shi and Ke Mao contributed equally to this work.

✉ Yang Yue, yueyang@ahu.edu.cn; Yihua Gao, gaoyihua@hust.edu.cn

1. Wuhan National Laboratory for Optoelectronics (WNLO) and School of Physics, Center for Nanoscale Characterization & Devices (CNCD), Huazhong University of Science and Technology (HUST), Wuhan 430074, People's Republic of China

2. Guangxi Key Laboratory of Optical and Electronic Materials and Devices, College of Materials Science and Engineering, Guilin University of Technology, Guilin 541004, People's Republic of China

3. Hong Kong Center for Cerebro-Cardiovascular Health Engineering, Hong Kong SAR 999077, People's Republic of China

4. Hubei Key Laboratory of Critical Materials of New Energy Vehicles and School of Mathematics, Physics and Optoelectronic Engineering, Hubei University of Automotive Technology, Shiyan 442002, People's Republic of China

5. Information Materials and Intelligent Sensing Laboratory of Anhui Province, Key Laboratory of Structure and Functional Regulation of Hybrid Materials of Ministry of Education, Institutes of Physical Science and Information Technology, Anhui University, Hefei 230601, People's Republic of China

1 Introduction

Up to now, many remote areas still do not have developed power grid or access to environmentally sound and affordable energy [1, 2]. Therefore, the development of self-charging power systems is very significant to solve the problem of energy poverty in underdeveloped areas. To solve this problem, the integrated systems have been developed, combining rechargeable battery (e.g., alkali batteries, zinc ion batteries (ZIBs)) with external energy collection systems (e.g., solar cells, thermobatteries, nanogenerators) [3–8]. However, under certain conditions, external energy collection systems are not always sustainable access, for example, solar cells need sunlight, thermobatteries need temperature difference and nanogenerators need additional mechanical energy [9–11]. In addition, the complex and large component of the integrated self-charging power systems is not suitable for the rapid development of portable and wearable electronics. Therefore, it is necessary to find a new type of self-charging power systems with simplified configuration and suitable for various environments.

Oxygen is known to be a rich source of energy from air and can be used to convert chemical energy into electrical energy through redox reactions. Therefore, combining the chemical energy of oxygen with the electrochemical energy of electrode material is an effective method to obtain self-charging batteries. Considering the instability of alkali batteries in the air [12–16], aqueous batteries seem to be the only option for self-charging batteries. In particular, ZIBs have recently stood out because the Zn anode possesses inherent merits such as high capacity (820 mAh g^{-1}), low redox potential (-0.76 V vs. SHE), high safety, environmental benignity and low cost [17–23].

At present, some researches have been made in the combination of ZIBs and oxygen to produce air-rechargeable ZIBs. For example, Chen et al. at first reported a air-rechargeable ZIBs based on GaVO cathodes, which can be charged by oxygen for 36 h to reach 1.05 V open-circuit voltage, providing a capacity of 239 mAh g^{-1} at 0.1 A g^{-1} [24]. However, the air-rechargeable ZIBs show limited cycle life (only five cycles), so the exploration of ZIBs with higher life was the next logical step. Subsequently, Wang et al. reported a air-rechargeable ZIBs based on poly(1,5-naphthaleneamine) cathode and alkaline electrolyte. Benefited from the weak coordination reaction between the cathode and cation, the

cycle life of air-rechargeable ZIBs is improved (100 cycles). However, its discharge capacity is only 186 mAh g^{-1} at 0.2 A g^{-1} [25]. These works undoubtedly provide an effective strategy for the development of air-rechargeable ZIBs. However, it is still necessary to develop new air-rechargeable cathodes to obtain air-rechargeable ZIBs with both long life and high capacity.

As well known, among many ZIBs cathodes materials, organic–inorganic hybrid materials (OIHMs) have long cycle life and high capacity, benefiting from that organics can manage to enhance the electronic transfer, suppress the cathode dissolution and moderate the charge-shielding effect of Zn^{2+} [26–34]. Therefore, OIHMs are considered as the alternatives to cathodes, which evokes a new topic of whether these OIHMs can be used to fabricate air-rechargeable ZIBs. In particular, the most of reported OIHMs with higher reduction potential (> 0.9 V vs. Zn/Zn^{2+}) such as V_2O_5/PANI [26, 27], $C_2H_8N_2V_7O_{16}$ [28], MnO_2/PANI [29], V_2O_5@PEDOT [30], PEDOT-$NH_4V_3O_8$ [31], NVO-PEDOT [32], VO_2/PPy [33] and VOPO$_4$/PA [34] are not conducive to fast and reliable air recharging by oxygen. Therefore, up to now, the air-rechargeable performance of OIHMs with the presence of oxygen has never been reported.

Herein, we propose an air-rechargeable ZIB based on polyaniline-coated MoS_2 cathodes (MoS_2/PANI). The introduction of conductive polymer (PANI) coating of MoS_2 not only improves the conductivity, but also induces the charge redistribution and structure changes at the interface to weaken the electrostatic interaction, thus promoting the diffusion of Zn^{2+}. Accordingly, MoS_2/PANI cathodes show the best electrochemical performance of zinc ion storage (304.98 mAh g^{-1} in N_2 and 351.25 mAh g^{-1} in air at 0.50 A g^{-1}) among the MoS_2-based cathodes so far [25–42]. More importantly, the ex situ characterization of MoS_2/PANI and MoS_2 proved that PANI coated on MoS_2 surface could play a desolvation role, which enables MoS_2/PANI materials to have great capacity and minimal lattice strain in the discharging process. Benefited from the low reduction potential of the MoS_2/PANI cathodes (0.71 V vs. Zn/Zn^{2+}), the ZIB can be quickly and deeply air recharged by oxygen (316.09 mAh g^{-1} at 0.50 A g^{-1} after 24-h air recharging, i.e., 89.99% capacity retain of galvanostatic charge at 0.50 A g^{-1}) and have long air recharging/galvanostatic discharging life (50 cycles). As a proof

of concept, the quasi-solid zinc ion batteries (QSZIBs) assembled by MoS_2/PANI cathode, zinc nanoflakes anode and polyacrylamide/polyethylene glycol/zinc trifluoromethanesulfonic acid (PAM/PEG/$Zn(CF_3SO_3)_2$) hydrogel electrolyte demonstrates great electrochemical performance, excellent flexibility, high- and low-temperature stability and air-recharging ability. Finally, to further verify their practicality, a 3×3 battery module was successfully assembled and powered a pressure sensor and a smartphone. This work will provide a promising research direction for the material design and device assembly of the next-generation self-powered system.

2 Results and Discussion

2.1 Design Principle and Structural Characterizations

The structure design, air recharging and galvanostatic discharging processes of the QSZIBs are shown in Fig. 1a. The QSZIBs consist of MoS_2/PANI cathode, zinc nanoflakes anode and PAM/PEG/$Zn(CF_3SO_3)_2$ hydrogel electrolyte. When discharged QSZIBs are exposed to air, Zn^{2+} was extracted from cathode in the presence of O_2 and H_2O. When QSZIBs is used to power the external circuit, the solvated Zn^{2+} moves from anode to cathode and is embedded into
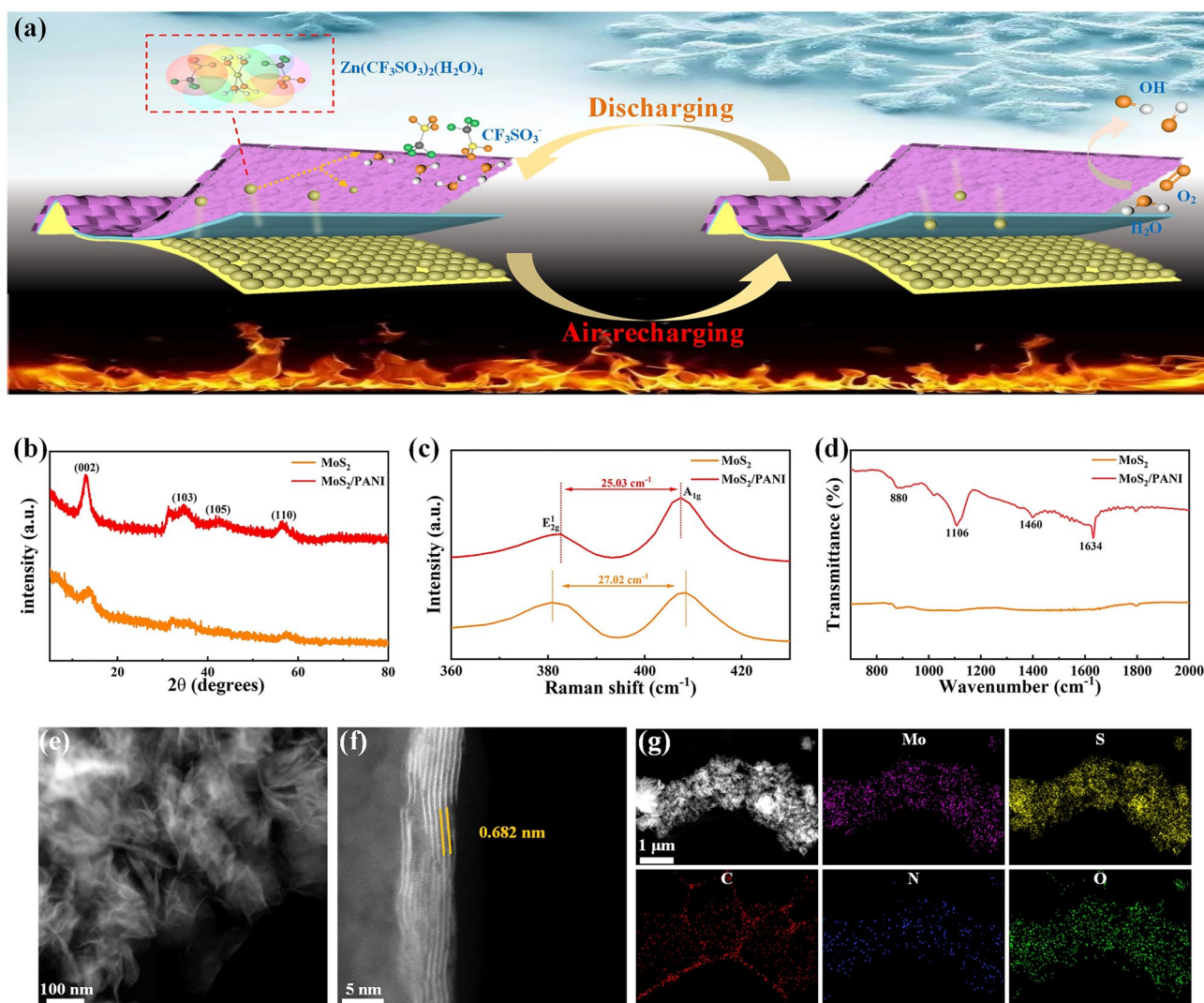

Fig. 1 Structure of air-rechargeable QSZIBs and characterization of MoS_2/PANI nanoflowers. **a** Structure of air-rechargeable QSZIBs, **b** XRD patterns, **c** Raman patterns and **d** FTIR spectrum of original MoS_2 and MoS_2/PANI. **e** Enlarged TEM image, **f** HTEM image and **g** STEM elemental mapping image of MoS_2/PANI nanoflowers

the cathode after being de-solvated on the cathode surface. The original MoS_2 and MoS_2/PANI nanoflowers were synthesized by simple hydrothermal method, and the successful synthesis was proved by a series of characterization. Figure 1b exhibits the X-ray diffraction (XRD) patterns of the original MoS_2 (JCPDS No. 37–1492) and MoS_2/PANI [43, 44]. It can be seen that compared with the original MoS_2, the peak of MoS_2/PANI shows a small angle shift, indicating that the most of PANI is coated on the surface of MoS_2 and only a very extreme amount of PANI enters in interlayer. However, the diffraction peaks of PANI are not observed in the samples (Fig. S1a), probably because only a very small amount of PANI was introduced in the MoS_2/PANI. The TG curves of MoS_2 and MoS_2/PANI in Fig. S2 indicate that the content of PANI in the MoS_2/PANI is 5.27 wt%. The Raman spectra of original MoS_2 and MoS_2/PANI are shown in Fig. 1c. The interval between the E_{2g}^1 and A_{1g} peaks of MoS_2/PANI decreased, indicating that the introduction of PANI weakened interaction between neighboring MoS_2 layers [35]. The FTIR and XPS results further confirmed the successful synthesis of MoS_2/PANI. As shown in Figs. 1d and S1b, the FTIR spectrum of MoS_2/PANI nanoflowers also shows the peaks related to PANI, but with some offsets due to the presence of MoS_2. As shown in Fig. S3, the full X-ray photoelectron spectrometer (XPS) spectrum of MoS_2/PANI shows the signal of Mo, S, O, C and N which are attributed to MoS_2 and PANI, respectively. As can be seen from the Mo 3d XPS spectra in Fig. S4a, the peak values of 228.9 and 232.1 eV with the spin energy separation of 3.2 eV were observed, which correspond to the Mo $3d_{5/2}$ and Mo $3d_{3/2}$ of Mo^{4+}, respectively [45], while the obvious peak at 236.2 eV is associated with the Mo^{6+} due to MoS_2 defects caused by the introduction of PANI. It is worth noting that there is also a weak Mo^{6+} peak in the original MoS_2 (Fig. S5a), which may be related to the incomplete decomposition of raw materials [36]. The XPS spectrums spectra were fitted to analyze the phase composition of the original MoS_2 and MoS_2/PANI, which are both composed of 1 T-phase and 2H-phase (Figs. S4b, S5b and Table S1). It is worth noting that the strain of lattice mismatch caused by a small amount of PANI entering the interlayer of MoS_2 is the reason that MoS_2/PANI contains more 1 T phases than the original MoS_2. The morphology and microstructure of original MoS_2, PANI and MoS_2/PANI were characterized by scanning electron microscopy (SEM). Compared with the original MoS_2 and PANI (Fig. S6a, b), the MoS_2/PANI

exhibits smaller and fluffier nanoflowers (Fig. S6c). The microstructure of original MoS_2, PANI and MoS_2/PANI was further studied by transmission electron microscopy (TEM). The PANI consisting of C and N shows an amorphous phase (Fig. S7). As can be seen from the TEM images of MoS_2/PANI nanoflowers in different magnifications in Figs. S8a and 1e, the MoS_2/PANI nanoflowers are assembled from nanosheets around 100 nm, which display much thinner and smaller nanoflowers than the original MoS_2 (Fig. S9a, b). As shown in Figs. 1f and S9c, the high-resolution TEM (HRTEM) images show that the layer spacing of MoS_2 (002) in MoS_2/PANI increased from 0.620 to 0.682 nm, indicating that an extreme small amount of PANI entered in MoS_2 layers, which is similar to the XRD results (Fig. 1b). Meanwhile, the HAADF-TEM images of original MoS_2 and MoS_2/PANI visually prove that the phase species are both composed of 1 T-phase and 2H-phase (Figs. S8d and S9d). Typical interfaces of MoS_2 and PANI are also observed in Fig. S8b-d, which provides compelling evidence for the coating of this PANI. The STEM elemental mapping image in Fig. 1g reveals the homogeneous distribution of Mo, S, C, N and O elements along the MoS_2/PANI nanoflowers.

2.2 Electrochemical Performances and Electrode Process Kinetic

The electrochemical performance of MoS_2/PANI was evaluated by a standard two-electrode system in air. The CV curves at 1.0 mV s^{-1} and GCD curves at 2.0 A g^{-1} of original MoS_2, PANI and MoS_2/PANI are shown in Figs. 2a, b and S10a, b. The MoS_2/PANI cathodes show the maximum CV area and specific capacity, indicating the excellent modification effect of PANI on MoS_2. The Nyquist plot, equivalent circuit and corresponding resistances of the original MoS_2, PANI and MoS_2/PANI are shown in Fig. S11a, b and Table S2, respectively, indicating that the introduction of PANI can effectively improve the electrochemical reaction kinetics of MoS_2. As shown in Fig. S12, we further studied the MoS_2/PANI cathodes with different amounts of PANI and found that both too high and too low amount of PANI lead to the deterioration of MoS_2/PANI performance, which may be due to the fact that more or less PANI is not conducive to the formation of MoS_2/PANI nanoflowers (Figs. S13 and S14). The specific capacity of the above samples was further tested at current densities
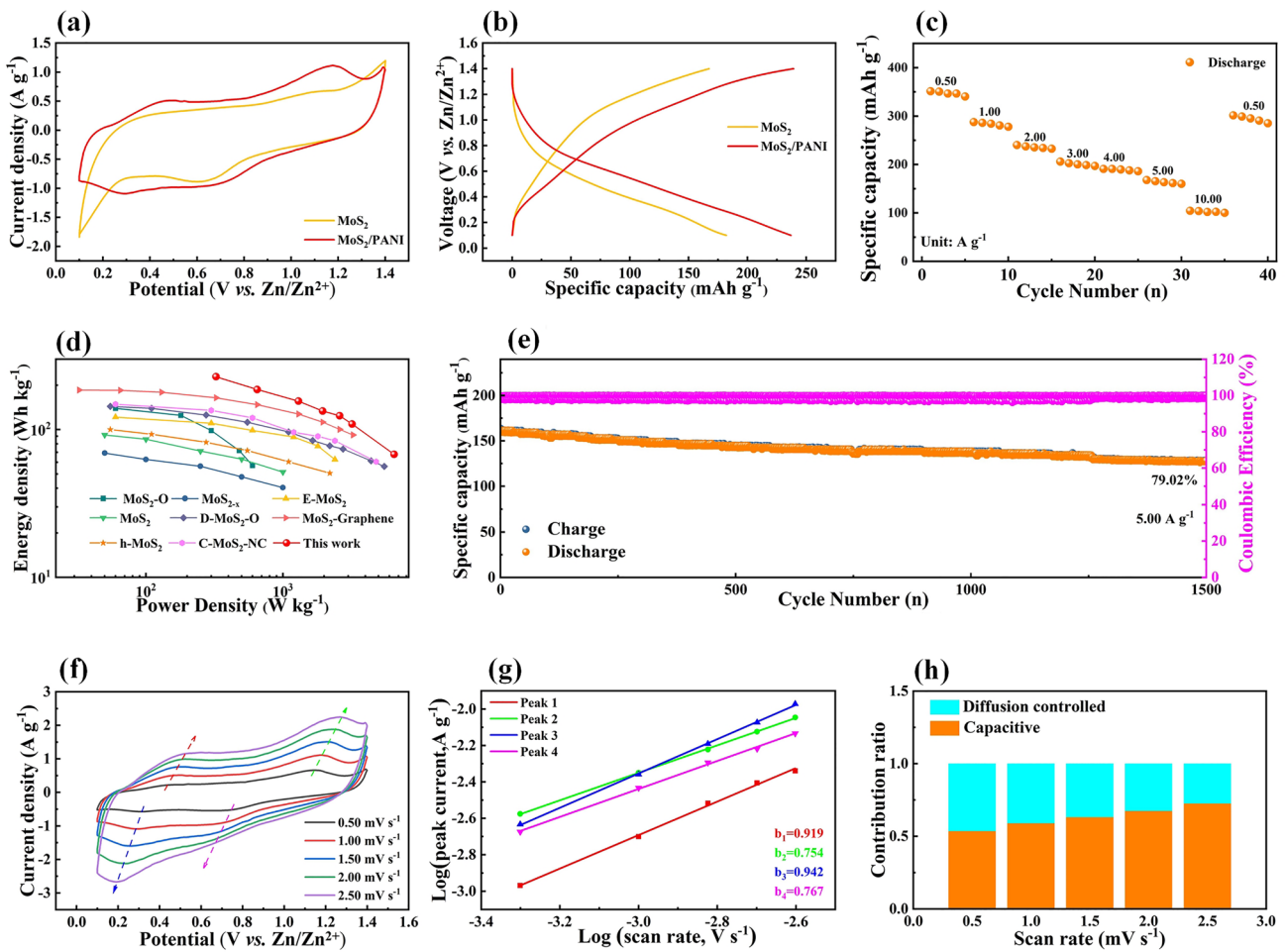
Fig. 2 Electrochemical performances and electrode process kinetic of MoS$_2$/PANI cathodes in air. **a** CV curves at a scan rate of 1.0 mV s^{-1} and **b** GCD curves at a current density of 2.0 A g^{-1} of the MoS$_2$/PANI cathodes and MoS$_2$ cathodes. **c** Rate capability, **d** energy and power density plot, **e** cyclic life and Coulomb efficiency and **f** CV curves at different scan rates from 0.50 to 2.50 mV s^{-1} of the MoS$_2$/PANI cathodes. **g** Log (i) versus log (v) plots and **h** contribution ratios of diffusion-controlled and capacitive capacities at different scan rates of the MoS$_2$/PANI cathodes

from 0.50 to 10.00 A g^{-1} (Figs. S15-S18 and 2c) to prove that MoS$_2$/PANI cathodes had the best electrochemical performance. In addition, Fig. 2c also shows the excellent rate capability of MoS$_2$/PANI cathode (the specific capacity at 0.50, 1.00, 2.00, 3.00, 4.00, 5.00 and 10.00 A g^{-1} is 351.25, 287.56, 239.93, 205.80, 190.84, 167.78 and 104.44 mAh g^{-1}, respectively). As notably highlighted in Fig. 2d, the MoS$_2$/PANI cathodes manifest higher energy densities over a wider power density range compared to the recently reported MoS$_2$-based cathodes for AZIBs, which has the power density and energy density as high as 6500.0 W kg^{-1} and 228.3 Wh kg^{-1}, respectively. To illustrate their excellent stability, the MoS$_2$/PANI cathodes were tested at a current density of 5.00 A g^{-1}. After

1500 charge/discharge cycles, the capacity retention rate of the MoS$_2$/PANI cathodes was 79.02% (Fig. 2e). The morphology and structure of MoS$_2$/PANI cathodes before and after the cycle were characterized by SEM to prove the stability of MoS$_2$/PANI cathodes. Figure S19b shows SEM images of MoS$_2$/PANI cathodes after 1500 GCD cycles (charged to 1.40 V), which are basically unchanged from original morphology and structure (Fig. S19a), indicating that the ion insertion/extraction behavior during the cycle is reversible.

Then the energy storage mechanism of MoS$_2$ and MoS$_2$/PANI was studied. As shown in Figs. 2f and S20a, the electrochemical reaction kinetics of MoS$_2$ and MoS$_2$/PANI cathodes were revealed by CV curves at different sweep rates

from 0.50 to 2.50 mV s^{-1}. The electrochemical reaction kinetics can be assessed by Eq. 1 [46, 47]:

$$i = av^b \qquad (1)$$

As shown in Figs. 2g and S20b, the b values reveal that the electrochemical reaction kinetics of both MoS$_2$ and MoS$_2$/PANI cathodes are composed of capacitive and diffusion controlled. At a specified scan rate, the capacitive contribution and the diffusion-controlled contribution can be further evaluated according to Eq. 2 [48, 49]:

$$i(v) = k_1 v + k_2 v^{1/2} \qquad (2)$$

As shown in Figs. 2h and S20c, with the increase in scan rate, the ratio of the capacitive contribution process increases gradually, and the capacitive process plays a leading role in

the total process. It is worth noting that the diffusion-controlled contribution of MoS$_2$/PANI is always greater than that of MoS$_2$ at all scan rates, indicating that the high capacity of MoS$_2$/PANI is mainly due to ion diffusion rather than ion adsorption (Fig. S21).

2.3 Galvanostatic Intermittent Titration Technique and Density Functional Theory

The reaction kinetics of MoS$_2$/PANI cathodes can be further studied by GITT (Fig. 3a) to estimate the Zn^{2+} diffusion coefficient (D_{Zn}). As shown in Fig. 3b, the D_{Zn} calculated by galvanostatic intermittent titration technique (GITT, calculation details are described in Experimental Section) in
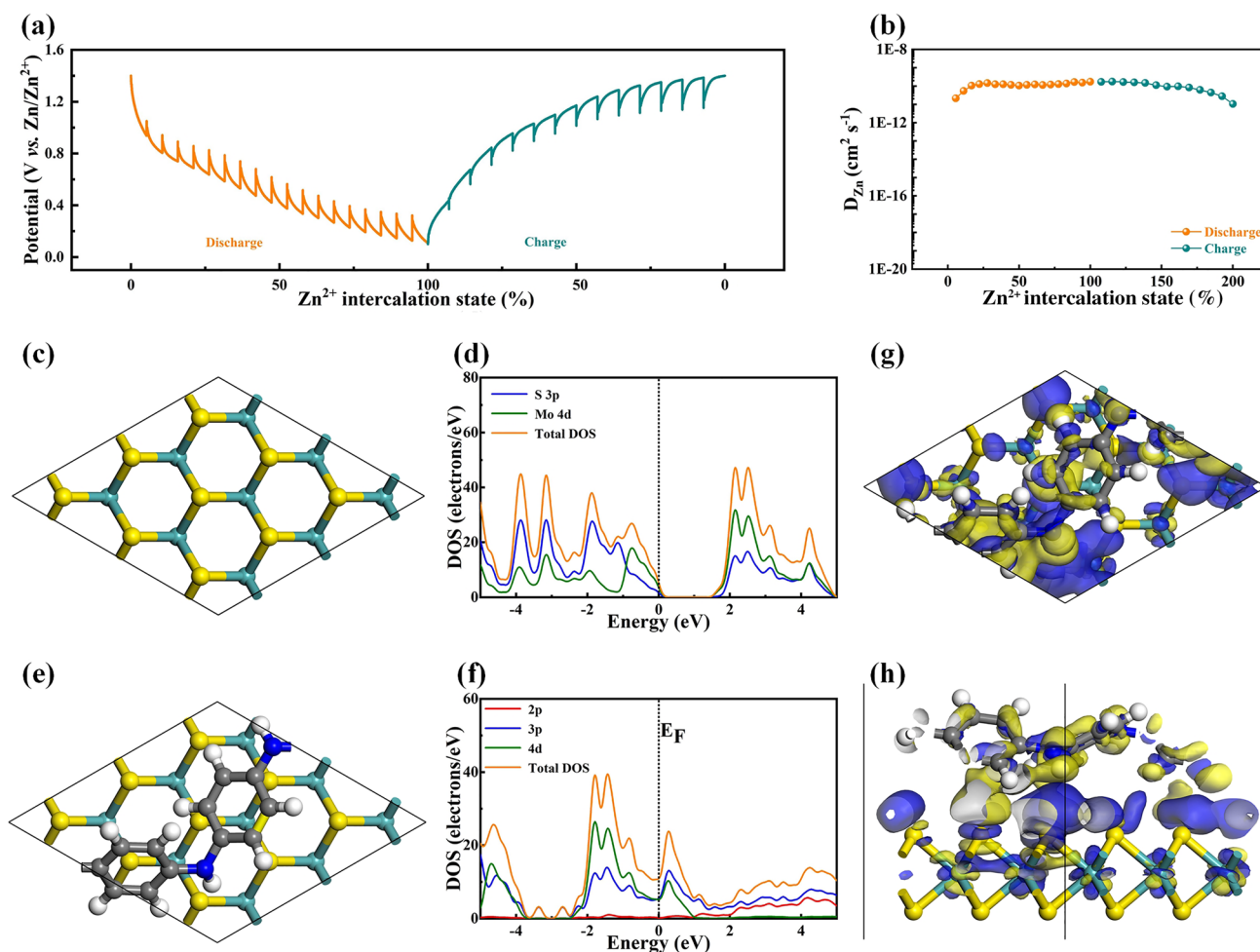

Fig. 3 GITT and DFT of MoS$_2$/PANI cathodes. **a** GITT and **b** D_{Zn} of MoS$_2$/PANI cathodes. **c** The initial model establishment of MoS$_2$ and **d** corresponding density map. **e** The model establishment of MoS$_2$/PANI and **f** corresponding density map. **g, h** The differential charge diagram of MoS$_2$/PANI

the charge and discharge process consistently reveals a D_{Zn} values range of 10^{-11}–10^{-9} cm^2 s^{-1}. The D_{Zn} values achieved in this work are higher than MoS$_2$ and previously reported manganese and vanadium-based oxide cathodes for AZIBs (Fig. S22 and Table S3). The reaction kinetics of MoS$_2$ and MoS$_2$/PANI were also studied by density functional theory (DFT) calculation. The disadvantage of MoS$_2$ as cathode material of ZIBs is its weak reaction kinetics due to its poor conductivity. The initial model establishment of MoS$_2$ and corresponding density map are shown in Fig. 3c, d, respectively. It can be seen that the original MoS$_2$ has a relatively large band gap, which is similar to the previous report [50–52]. Therefore, the transfer of electrons from valence to conduction band requiring a lot of energy indicates its poor conductivity, which limits its performance. The model establishment of MoS$_2$/PANI and corresponding density map are shown in Fig. 3e, f, respectively. It can be seen that the state density near the Fermi level of MoS$_2$/PANI increases, electrons are easier to transition from the valence band to the conduction band, and the introduction of PANI enhances the conductivity of MoS$_2$/PANI. As shown in Fig. 3g, h of differential charge diagram of MoS$_2$/PANI, the PANI and MoS$_2$ base have obvious charge transfer, which further indicates that PANI can have relatively strong interaction with MoS$_2$ after insertion. Therefore, after the incorporation of PANI, PANI will combine with the substrate material MoS$_2$ and further improve the conductivity of the material. In addition, DFT calculation also proves that the increase of the layer spacing reduces the zinc ion transport barrier from 0.99 to 0.39 eV (Fig. S23).

2.4 Energy Storage Mechanism

In order to clarify the energy storage mechanism, MoS$_2$/PANI cathode was tested in N$_2$ to exclude external interference factors (such as air recharging). As shown in Figs. S24 and S25, the MoS$_2$/PANI cathodes exhibit better cycling stability and lower capacity in N$_2$. However, for layered materials, the interlayer spacing determines the storage capacity of zinc ions (Fig. S26), so MoS$_2$/PANI cathodes may have some special energy storage mechanisms. In order to clarify the energy storage mechanism of MoS$_2$/PANI cathode, the structural evolution of the MoS$_2$/PANI cathode was characterized by ex situ XRD. The marked states (points A–E) during charge/discharge were selected for ex situ XRD

tests (Fig. 4a). When the MoS$_2$/PANI cathode discharged, the peak of (002) gradually shifts toward a smaller angle (Fig. 4b), reflecting the interlayer expansion caused by Zn^{2+}. During charging (from state A to state C), the peak of (002) gradually recovers to the initial position, indicating that the ions insertion/extraction of MoS$_2$/PANI cathode was highly reversible. It is worth noting that during the discharge process the peak of (002) moves very a little toward the lower angle, indicating that the interlayer expansion of MoS$_2$/PANI cathode during charging and discharging process is very small. Generally speaking, when materials are discharged, they exhibit small interlayer expansion mainly for the following reasons: (1) limited zinc ion embedding; (2) other small ions interlayer contribution capacity; (3) there is desolvation phenomenon. First, the Inductive Coupled Plasma Emission Spectrometer (ICP) analyses of MoS$_2$/PANI cathode at fully discharged and charged were tested. As shown in Table S4, the ratio of Zn to Mo atoms before and after MoS$_2$/PANI charging and discharging is 0.8474 and 0.0237, which proves that the capacity of MoS$_2$/PANI is mainly contributed by zinc ion intercalation. Then, we verify that the H$^+$ insertion has a little contribution to the cathode capacity (Fig. S27). However, the presence of Zn^{2+} in 2.0 M Zn(CF$_3$SO$_3$)$_2$ takes the form of larger Zn(CF$_3$SO$_3$)$_2$(H$_2$O)$_4$ (inserted form is Zn(H$_2$O)$_4$$^{2+}$), which usually causes larger interlayer expansion when inserted in electrode materials with smaller interlayer spacing [53–56]. Therefore, we supposed that when Zn(H$_2$O)$_4$$^{2+}$ is inserted in MoS$_2$/PANI cathode, there is a mechanism of desolvation on the surface of electrode material, which causes Zn(CF$_3$SO$_3$)$_2$(H$_2$O)$_4$ to change into smaller Zn^{2+}. Therefore, further tests were carried out to prove above conjecture and clarify the storage mechanism of MoS$_2$/PANI cathodes. The *ex situ* Raman spectra of MoS$_2$/PANI cathode at different charge and discharge states were collected (Fig. 4c). When MoS$_2$/PANI cathode was discharged to 0.10 V, the intensity ratio of A_{1g}/E^1_{2g} decreased (*A* and *E*), indicating that ions had been inserted into the interlayer of MoS$_2$/PANI cathode. When MoS$_2$/PANI cathode was charged to 1.40 V, the intensity ratio of A_{1g}/E^1_{2g} recovered to 1.47 due to the extraction of ions. The intensity ratio of A_{1g}/E^1_{2g} changes slightly during charging and discharging process of MoS$_2$/PANI cathode, which are consistent with the results of *ex situ* XRD. In order to prove that Zn^{2+} rather than other ions inserted MoS$_2$/PANI cathode, XPS spectrum of the original, fully discharged and charged states has been studied. As shown in Fig. 4d, no Zn signal
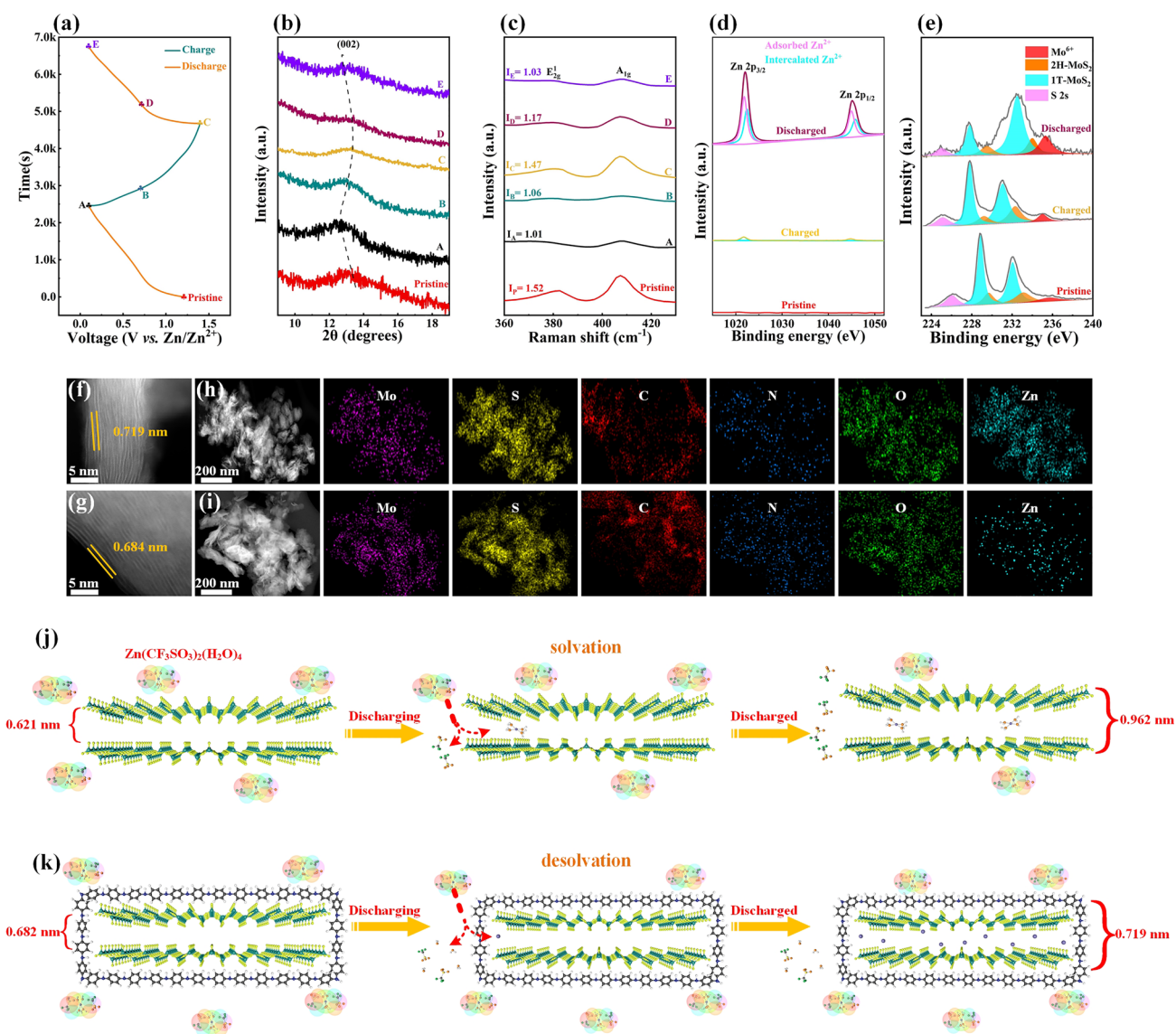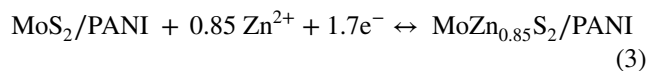
Fig. 4 Zn storage mechanism of MoS$_2$/PANI cathodes. **a** Initial discharge/charge curve at 0.50 A g^{-1}, the marked states are selected for ex situ tests. *Ex situ* **b** XRD patterns, **c** Raman patterns, XPS spectra of **d** Zn and **e** Mo. **f, g** HRTEM and **h, i** STEM element mapping images of the fully discharged and charged MoS$_2$/PANI cathodes. **j, k** The solvation and desolvation of MoS$_2$ and MoS$_2$/PANI

was detected in the Zn 2p XPS spectrum of the original electrode. When MoS$_2$/PANI cathode was fully discharged, two pairs of Zn 2p signals can be observed, corresponding to the Zn^{2+} absorbed on the electrode surface and the Zn^{2+} inserted in electrode, respectively. After fully charging to 1.40 V, a pair of weak Zn signals were still observed due to the adsorption of residual Zn(CF$_3$SO$_3$)$_2$. Spectra and fitting results of XPS in different states in Mo 3d of MoS$_2$/PANI cathode are shown in Fig. 4e and Table S1. The Mo 3d XPS deconvolution shows that the pristine electrode contains
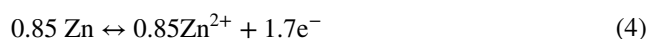
65.82% 1 T-MoS$_2$ and 29.18% 2H-MoS$_2$, along with 5.00% Mo^{6+} caused by surface oxidation. After being discharged to 0.10 V, the proportion of 2H-MoS$_2$ is reduced to 18.78% (against 65.74% for 1 T-MoS$_2$ and 15.48% for Mo^{6+}), illustrating the phase transition from 2H- to 1 T-MoS$_2$ induced by Zn^{2+} insertion. It is worth noticing that the 1 T-MoS$_2$ could be easily oxidized (during the XPS testing process), especially after electrochemical activation [29], which explains the dramatically strengthened Mo^{6+} signal and the reduced 1 T-phase content. After charging to 1.40 V,

the original content of 2H-MoS$_2$ is finely restored, indicating the highly reversible phase transition triggered by Zn^{2+} insertion/extraction. The reversible phase transition between 1 T-MoS$_2$ and 2H-MoS$_2$ during Zn^{2+} insertion/extraction was confirmed. The *ex situ* HRTEM image (Fig. 4f, g) visually shows the fringe distance of 0.719/0.684 nm at the insertion/extraction of Zn^{2+}, which is in good agreement with the XRD results. STEM elemental mapping images reveal the uniform distribution of Mo, S, C, N, O and Zn elements in the fully discharged electrode (Fig. 4h) and fully charged electrode (Fig. 4i), indicating the reversible insertion/extraction of Zn^{2+}. Based on the above discussion, the storage mechanism of MoS$_2$/PANI cathode is summarized as the reversible insertion/extraction of Zn^{2+} formed by the desolvation of Zn(CF$_3$SO$_3$)$_2$(H$_2$O)$_4$ on the electrode surface rather than Zn(H$_2$O)$_4$$^{2+}$. To investigate whether PANI plays an important role in the desolvation of Zn(CF$_3$SO$_3$)$_2$(H$_2$O)$_4$, the Zn storage mechanism of the original MoS$_2$ electrode has also been studied (Figs. S28 and S29). It is found that the peak of (002) has obvious shift to lower angle and the layer spacing increases to 0.962 nm. In addition, it is noteworthy that no significant change in the peak intensity of F 1 *s* XPS spectrum was detected in the full charging and discharging of original MoS$_2$ and MoS$_2$/PANI cathode, indicating that CF$_3$SO$_3$$^{2-}$ really did not inserted in the electrode and the detected F 1 *s* spectra were attributed to the adsorption of electrolyte (Fig. S30). However, when the original MoS$_2$ cathode was fully charged and discharged, the detected O 1 *s* XPS spectral peak intensity changed significantly, indicating that Zn(H$_2$O)$_4$$^{2+}$ may be inserted into the electrode (Fig. S31). Energy storage mechanism of original MoS$_2$ and MoS$_2$/PANI cathode in discharge process is shown in Fig. 4j, k. For the original MoS$_2$, Zn(H$_2$O)$_4$$^{2+}$ formed by thedecomposition of Zn(CF$_3$SO$_3$)$_2$(H$_2$O)$_4$ on the surface of MoS$_2$ was directly inserted into MoS$_2$, resulting the layer spacing increases. For MoS$_2$/PANI cathode, Zn(CF$_3$SO$_3$)$_2$(H$_2$O)$_4$ will first form coordination with PANI on the surface. Benefits from the synergistic effect of Zn^{2+} and π electrostatic interaction, the solvent shell around the Zn^{2+} will collapse in the transmission process [57, 58]. Finally, Zn^{2+} are separately extracted into the cathode material through PANI (Fig. S32). Therefore, MoS$_2$/PANI cathode has a very small layer spacing increases after discharge and provides a very large capacity. Based on the above results and discussion, the overall electrochemical reaction of the ZIBs based on MoS$_2$/PANI cathode can be described as follows:

Cathode:

$$MoS_2/PANI + 0.85\ Zn^{2+} + 1.7e^- \leftrightarrow MoZn_{0.85}S_2/PANI \tag{3}$$

Anode:

$$0.85\ Zn \leftrightarrow 0.85Zn^{2+} + 1.7e^- \tag{4}$$

Overall:

$$MoS_2/PANI + 0.85\ Zn \leftrightarrow MoZn_{0.85}S_2/PANI \tag{5}$$

2.5 Air-Rechargeable Mechanism

The MoS$_2$/PANI cathode exhibits excellent Zn^{2+} storage performance, and the Mo was reduced/oxidized during the insertion/extraction of Zn^{2+}. During electrochemical charging, electrons are released from the MoZn$_{0.85}$S$_2$/PANI (Zn$_{0.85}$Mo/P) cathode and Mo in Zn$_{0.85}$Mo/P was oxidized and Zn^{2+} was extracted from the layered structure. In this process, the driving force for Zn$_{0.85}$Mo/P to release electrons is generally an external power supply. In addition to the above electrochemical oxidation reactions, other strategies that can realize electron transfer are also expected to be used in the charging process of air-rechargeable ZIBs based on Zn$_{0.85}$Mo/P cathode. Among various oxidants, O$_2$ is common and abundant in air and has the standard electrode potentials of ~0.40 and ~1.23 V *vs.* SHE in the neutral and acidic medium, respectively. Therefore, if the redox potential of Zn$_{0.85}$Mo/P cathode is lower than O$_2$, the oxidation of Mo and the extraction of Zn^{2+} of Zn$_{0.85}$Mo/P cathode can be realized. In order to verify the spontaneity of the redox reaction between Zn$_{0.85}$Mo/P and O$_2$ in 2.0 M Zn(CF$_3$SO$_3$)$_2$ electrolyte, a galvanic cell was designed. As shown in Fig. 5a, the Zn$_{0.85}$Mo/P electrode served as anode with 2.0 M Zn(CF$_3$SO$_3$)$_2$ electrolyte and was sealed under N$_2$ to avoid the dissolvation of oxygen. The platinum sheet was used as cathode, which was immersed in 2.0 M Zn(CF$_3$SO$_3$)$_2$ electrolyte containing dissolved oxygen. In this system, a cell voltage of 0.499 V was observed. According to the relationship between thermodynamic function and cell voltage:

$$\Delta G = -nEF \tag{6}$$

where ΔG, F, E and n are the Gibbs free energy change, Faraday constant cell voltage and normal number, respectively, the Gibbs free energy change of above system is less than zero, indicating that the redox reaction between Zn$_{0.85}$Mo/P
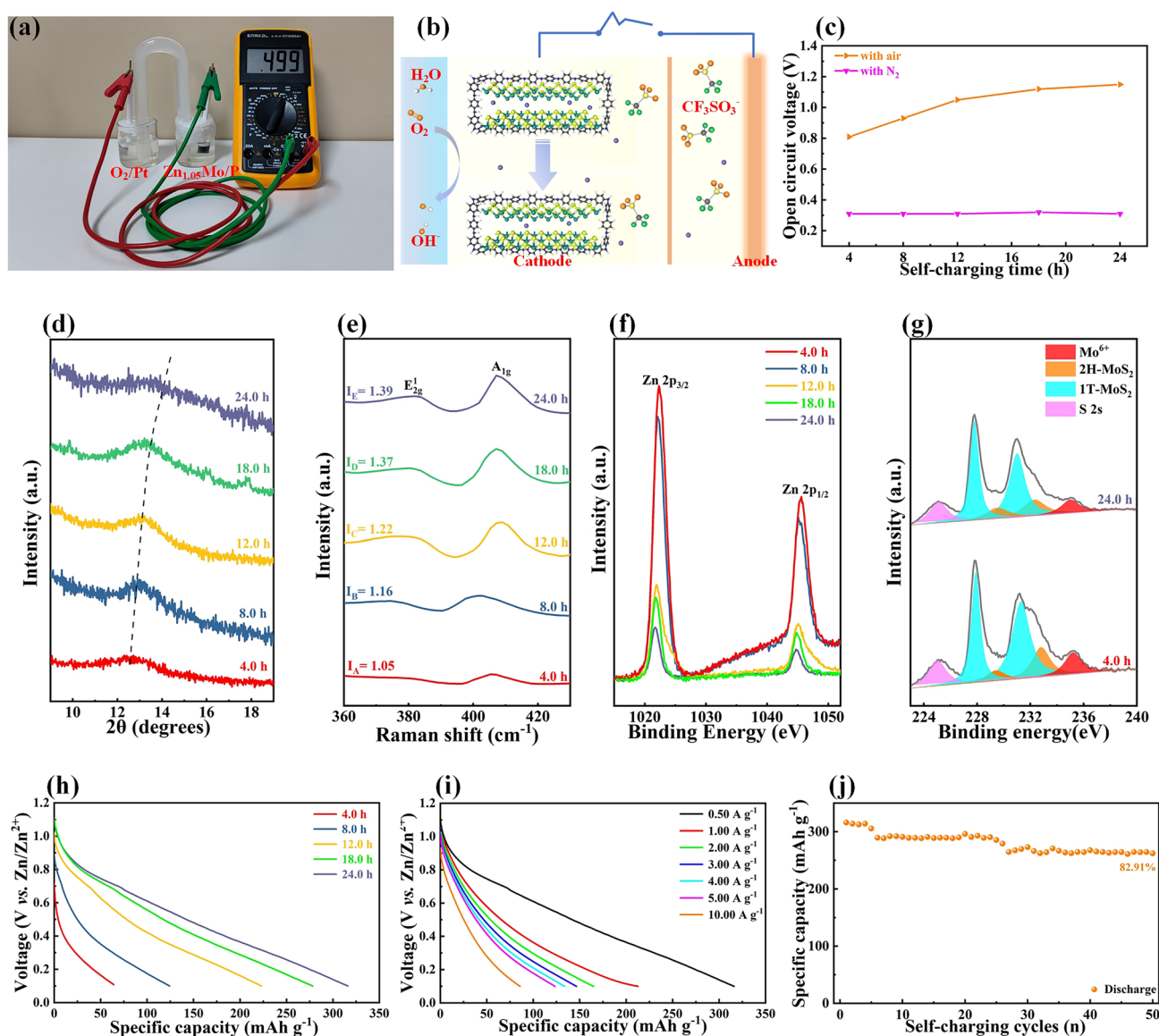
Fig. 5 Mechanism of the redox reaction between $Zn_{0.85}Mo/P$ and O_2 and air recharging/galvanostatic discharging behavior of $Zn//Zn_{0.85-x}Mo/P$ batteries. **a** Optical image of the designed galvanic cell. **b** Working mechanism of air-rechargeable ZIBs. **c** Effect of the oxidation time on OCV of $Zn//Zn_{0.85-x}Mo/P$ batteries. **d** XRD patterns, **e** Raman patterns, XPS spectra of **f** Zn and **g** Mo of $Zn//Zn_{0.85-x}Mo/P$ batteries after different air-recharging time. **h** Galvanostatic discharging curves of $Zn//Zn_{0.85-x}Mo/P$ batteries after different air-recharging time. **i** Galvanostatic discharging curves of $Zn//Zn_{0.85-x}Mo/P$ batteries at different current density after 24.0-h air recharging. **j** Air recharging/galvanostatic discharging life of $Zn//Zn_{0.85-x}MoS$ batteries

and O_2 can take place spontaneously in 2.0 M $Zn(CF_3SO_3)_2$. The air-recharging mechanism of ZIBs based on $Zn_{0.85}Mo/P$ cathode is shown in Fig. 5b. Under the action of O^2, Zn^{2+} is extracted from $Zn_{0.85}Mo/P$, while O_2 gains electrons from $Zn_{0.85}Mo/P$ and reacts with H_2O to form OH^-. The generated OH^- and extracted Zn^{2+} combine with the adsorbed electrolyte ions (Zn^{2+} and $CF_3SO_3^{2-}$) to form an amorphous trifluoride containing $Zn_{x+y}(CF_3SO_3)_{2y}(OH)_{2x}$ [Figs.

S33-S35] [18]. Therefore, the fully discharged $Zn_{0.85}Mo/P$ cathode can be restored to the charged state $Zn_{0.85-x}Mo/P$ cathode through spontaneous redox reaction. Subsequently, the curve of open-circuit voltage (OCV) with and without O_2 as a function of air-recharging time was tested (Fig. 5c), which further prove that O_2 plays an important role. More importantly, it is found that after 24.0 h of oxidation, the OCV of the ZIBs reached 1.15 V, close to the initial OCV

(1.21 V). In order to demonstrate the above mechanisms, ex situ characterization was carried out to study the structure and composition evolution of $Zn_{0.85-x}Mo/P$ electrodes. As the air-rechargeable time is extended from 0 to 24.0 h, the XRD peak (002) of $Zn_{0.85-x}Mo/P$ electrodes gradually shifts to a large angle (Fig. 5d), and the intensity ratio of A_{1g}/E^1_{2g} in Raman spectrum increases from 1.05 to 1.39 (Fig. 5e). This result is similar to that of chemical charging, indicating that Zn^{2+} gradually extracted from $Zn_{0.85-x}Mo/P$ electrode. In order to further prove the air-recharging mechanism of $Zn_{0.85-x}Mo/P$ electrode, XPS was carried out. With the increases of air-recharging time, the content of Zn in $Zn_{0.85-x}Mo/P$ electrode gradually decreased (Fig. 5f) and the Mo $3d$ peak gradually moved to a higher binding energy (Fig. 5g), indicating the gradual extraction of Zn^{2+} and oxidation of Mo in $Zn_{0.85-x}Mo/P$ cathode during the air-recharging process. The above discussion proves that the air-rechargeable ZIB based on $Zn_{0.85-x}Mo/P$ cathode can be charged by O_2. In order to determine the air-recharging performance of ZIB based on $Zn_{0.85-x}Mo/P$ cathode, the galvanostatic current discharge curves after air recharging for different times were tested (Fig. 5h). Since the air-rechargeable battery needs to consume zinc electrodes continuously during its operation, the mass of the zinc anode is strictly controlled at 21.2 mg to assemble the battery for practicability. After air recharging for 4.0 h, the corresponding discharge capacity of the ZIB can reach to 64.17 mAh g^{-1} at 0.50 A g^{-1}. As the air-recharging time increases, the capacity of the ZIB gradually increases. [35] Rechargeable ZIB could provide 316.09, 212.69, 164.94, 146.50, 133.61, 123.47 and 85.83 mAh g^{-1} at the current densities of 0.50, 1.00, 2.00, 3.00, 4.00, 5.00 and 10.00 A g^{-1}, respectively. As shown in Fig. S36, the air-rechargeable ZIB manifests high energy densities over a wider power density range which has the
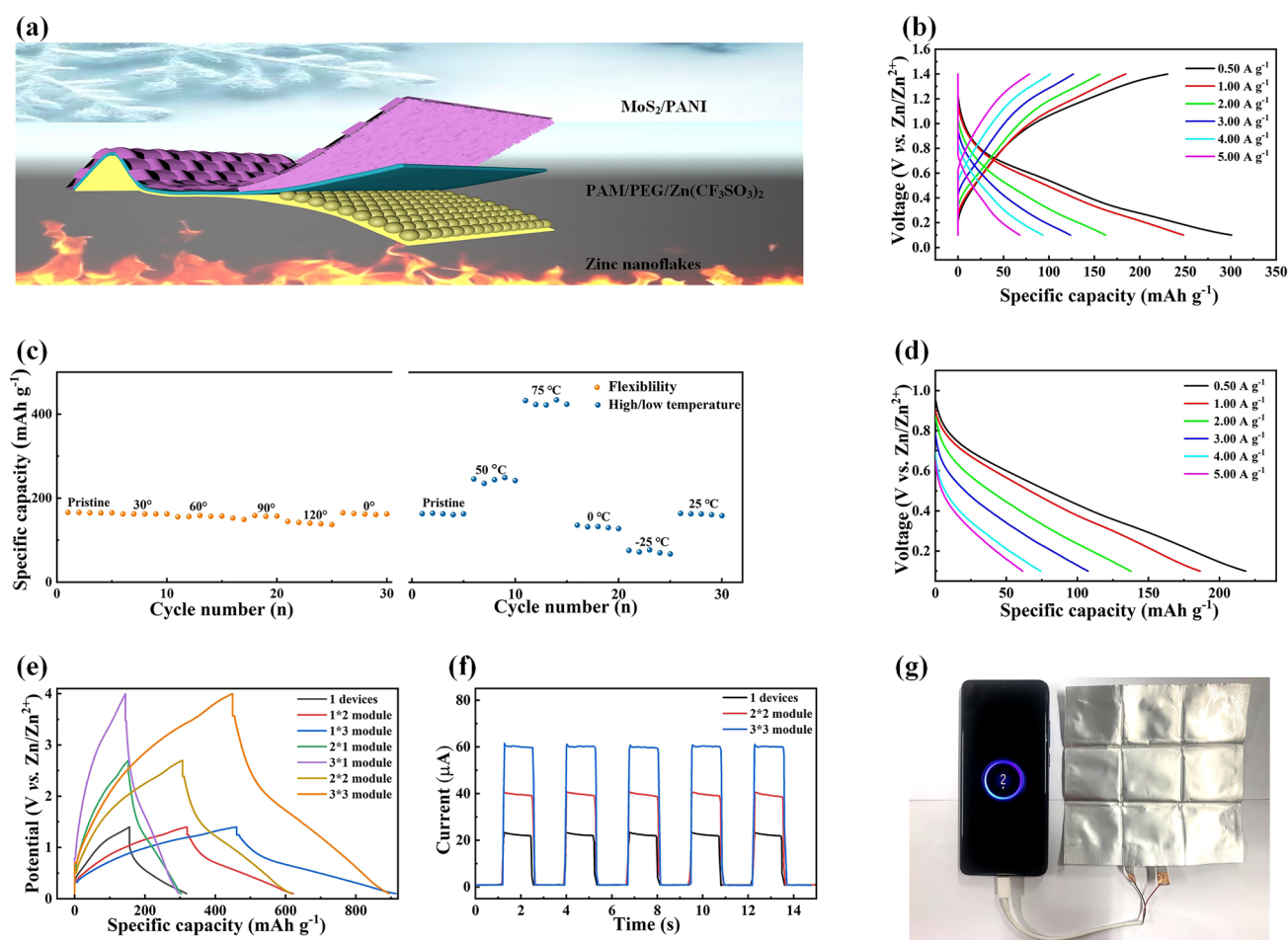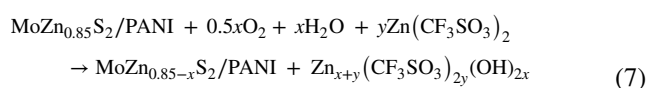

Fig. 6 Practicability of MoS$_2$/PANI cathode. **a** Schematic diagram and **b** GCD curves of the QSZIBs. **c** Specific capacity at 2.00 A g^{-1} of QSZIBs under bent or high and low temperatures. **d** Galvanostatic discharging curves of QSZIBs after 24.0-h air recharging. **e** GCD curves at 2.0 A g^{-1} of QSZIB module. The QSZIB module powered for **f** pressure sensors and **g** smartphones

power density and energy density as high as 288.29 W kg^{-1} and 12.69 Wh kg^{-1}, respectively. The stability of this air recharging/galvanostatic current discharge cycle was subsequently verified. In this test, the air-recharging ZIB based on $Zn_{0.85-x}$Mo/P cathode was discharged to 0.10 V at a current density of 0.50 A g^{-1} and then air recharged for 24.0 h and galvanostatic discharge at 0.50 A g^{-1}. As shown in Fig. 5j, the air-rechargeable ZIB can be cycled for 50 times. Afterward, the air-rechargeable ZIB shows a high discharge capacity of 291.22 mAh g^{-1} with the high capacity retention rate of 82.91%. Based on the above discussion, the redox reaction between $Zn_{0.85}$Mo/P and O_2 can be summarized as below:

$$MoZn_{0.85}S_2/PANI + 0.5xO_2 + xH_2O + yZn(CF_3SO_3)_2$$
$$\rightarrow MoZn_{0.85-x}S_2/PANI + Zn_{x+y}(CF_3SO_3)_{2y}(OH)_{2x} \tag{7}$$

2.6 Practicability and Zn Batteries Module

In order to illustrate the practicability of MoS_2/PANI cathode, QSZIBs were assembled by MoS_2/PANI cathode, zinc nanoflakes synthesized on carbon cloth by electrodeposition (Fig. S37) to assemble the battery for practicability. Anode and PAM/PEG/$Zn(CF_3SO_3)_2$ served as hydrogel electrolyte (Fig. 6a). As shown in Fig. 6b, the QSZIB shows excellent electrochemical performance. The discharge capacities at 0.50, 1.00, 2.00, 3.00, 4.00 and 5.00 A g^{-1} are 300.96, 248.04, 162.47, 123.63, 93.44 and 68.06 mAh g^{-1}, respectively. Considering that batteries often need to be operated in extreme conditions, QSZIB was tests under bent or high and low temperatures (Fig. 6c). The QSZIB shows only slight capacity variation under different bending states, indicating the excellent flexibility of the battery. Even more impressively, the QSZIB demonstrated high capacity and stability at both high and low temperature, respectively. Subsequently, the air-recharging ability of QSZIB was verified. After air recharging for 24.0 h, the fully discharged QSZIB shows a high capacity at different current densities (Fig. 6d). Considering the low capacity and voltage of QSZIB caused by the inherent characteristics of water batteries, a 3×3 module was constructed to further verify the practicality (Fig. 6e). In subsequent tests, the module was found to successfully power pressure sensors (Fig. 6f) and smartphones (Fig. 6g), showing great practical prospects.

3 Conclusions

In summary, we design a air-rechargeable ZIB based on MoS_2/PANI cathode. The introduction of conductive polymer (PANI) coating of MoS_2 not only improves the conductivity, but also induces the charge redistribution and structure changes at the interface to weaken the electrostatic interaction, thus promoting the diffusion of Zn^{2+}. Accordingly, MoS_2/PANI cathodes show the best electrochemical performance of zinc ion storage among the Mo-based cathodes so far. Benefited from the low reduction potential of the MoS_2/PANI cathodes (0.71 V vs. Zn/Zn^{2+}), the ZIBs can be quickly and deeply air recharged by oxygen (316.09 mAh g^{-1} at 0.50 A g^{-1} after 24-h air recharge, *i.e.,* 89.99% capacity retain of galvanostatic charge at 0.50 A g^{-1}) and have long air recharging/galvanostatic discharging life (50 cycles). As a proof of concept, the quasi-solid-state ZIBs employing MoS_2/PANI cathode and PAM/PEG/$Zn(CF_3SO_3)_2$ demonstrate great electrochemical performance, excellent flexibility, high- and low-temperature stability and air-rechargeable ability. Finally, to verify the practicality of the battery, a 3×3 battery module was successfully assembled to power a pressure sensor and a smartphone. This work will provide a promising research direction for the material design and device testing of the next-generation self-powered system.

References

1. G. Zichittella, J. Perez-Ramirez, Status and prospects of the decentralised valorisation of natural gas into energy and energy carriers. Chem. Soc. Rev. **50**(5), 2984–3012 (2021). https://doi.org/10.1039/d0cs01506g

2. P. Veers, K. Dykes, E. Lantz, S. Barth, C.L. Bottasso et al., Grand challenges in the science of wind energy. Science **366**(6464), 443 (2019). https://doi.org/10.1126/science.aau2027

3. Z. Li, Y. Gao, Z. Zhang, Q. Xiong, L. Deng et al., cPCN-regulated SnO$_2$ composites enables perovskite solar cell with efficiency beyond 23%. Nano-Micro Lett. **13**, 101 (2021). https://doi.org/10.1007/s40820-021-00636-0

4. N. Zhang, F. Huang, S. Zhao, X. Lv, Y. Zhou et al., Photo-rechargeable fabrics as sustainable and robust power sources for wearable bioelectronics. Matter **2**(5), 1260–1269 (2020). https://doi.org/10.1016/j.matt.2020.01.022

5. P. Peng, J. Zhou, L. Liang, X. Huang, H. Lv et al., Regulating thermogalvanic effect and mechanical robustness via redox ions for flexible quasi-solid-state thermocells. Nano-Micro Lett. **14**, 81 (2022). https://doi.org/10.1007/s40820-022-00824-6

6. Z. Li, Y. Xu, L. Wu, Y. An, Y. Sun et al., Zinc ion thermal charging cell for low-grade heat conversion and energy storage. Nat. Commun. **13**, 132 (2022). https://doi.org/10.1038/s41467-021-27755-x

7. Q. Zhang, Q. Liang, D.K. Nandakumar, H. Qu, Q. Shi et al., Shadow enhanced self-charging power system for wave and solar energy harvesting from the ocean. Nat. Commun. **12**, 616 (2021). https://doi.org/10.1038/s41467-021-20919-9

8. K. Zhao, Y. Wang, L. Han, Y. Wang, X. Luo et al., Nanogenerator-based self-charging energy storage devices. Nano-Micro Lett. **11**, 19 (2019). https://doi.org/10.1007/s40820-019-0251-7

9. P. Chen, T.T. Li, Y.B. Yang, G.R. Li, X.P. Gao, Coupling aqueous zinc batteries and perovskite solar cells for simultaneous energy harvest, conversion and storage. Nat. Commun. **13**, 64 (2022). https://doi.org/10.1038/s41467-021-27791-7

10. X. Wang, Y.T. Huang, C. Liu, K. Mu, K.H. Li et al., Direct thermal charging cell for converting low-grade heat to electricity. Nat. Commun. **10**, 4151 (2019). https://doi.org/10.1038/s41467-019-12144-2

11. G. Conta, A. Libanori, T. Tat, G. Chen, J. Chen, Triboelectric nanogenerators for therapeutic electrical stimulation. Adv. Mater. **33**(26), 2007502 (2021). https://doi.org/10.1002/adma.202007502

12. T. Liu, J. Wang, Y. Xu, Y. Zhang, Y. Wang, Dendrite-free and stable lithium metal battery achieved by a model of stepwise lithium deposition and stripping. Nano-Micro Lett. **13**, 170 (2021). https://doi.org/10.1007/s40820-021-00687-3

13. H. He, H. Zhang, D. Huang, W. Kuang, X. Li et al., Harnessing plasma-assisted doping engineering to stabilize metallic phase MoSe$_2$ for fast and durable sodium-ion storage. Adv. Mater. **34**(15), 2200397 (2022). https://doi.org/10.1002/adma.202200397

14. Q. Xiong, H. He, M. Zhang, Design of flexible films based on kinked carbon nanofibers for high rate and stable potassium-ion storage. Nano-Micro Lett. **14**, 47 (2022). https://doi.org/10.1007/s40820-022-00791-y

15. L. Zhao, Z. Liu, D. Chen, F. Liu, Z. Yang et al., Laser synthesis and microfabrication of micro/nanostructured materials toward energy conversion and storage. Nano-Micro Lett. **13**, 49 (2021). https://doi.org/10.1007/s40820-020-00577-0

16. Y. Gao, Z. Pan, J. Sun, Z. Liu, J. Wang, High-energy batteries: beyond lithium-ion and their long road to commercialisation. Nano-Micro Lett. **14**, 94 (2022). https://doi.org/10.1007/s40820-022-00844-2

17. X. Li, Y. Ma, Y. Yue, G. Li, C. Zhang et al., A flexible Zn-ion hybrid micro-supercapacitor based on MXene anode and V$_2$O$_5$ cathode with high capacitance. Chem. Eng. J. **428**, 130965 (2022). https://doi.org/10.1016/j.cej.2021.130965

18. D. Lin, Y. Li, Recent advances of aqueous rechargeable zinc-iodine batteries: challenges, solutions, and prospects. Adv. Mater. **34**(23), 2108856 (2022). https://doi.org/10.1002/adma.202108856

19. S. Zhao, X. Luo, Y. Cheng, Z. Shi, T. Huang et al., A flexible zinc ion hybrid capacitor integrated system with layers-dependent V$_2$CT$_x$ MXene. Chem. Eng. J. **454**, 140360 (2023). https://doi.org/10.1016/j.cej.2022.140360

20. D. Adekoya, S. Qian, X. Gu, W. Wen, D. Li et al., DFT-guided design and fabrication of carbon-nitride-based materials for energy storage devices: a review. Nano-Micro Lett. **13**, 13 (2020). https://doi.org/10.1007/s40820-020-00522-1

21. K. Chen, S. Kim, M. Je, H. Choi, Z. Shi et al., Ultrasonic plasma engineering toward facile synthesis of single-atom M-N$_4$/N-doped carbon (M = Fe, Co) as superior oxygen electrocatalyst in rechargeable zinc-air batteries. Nano-Micro Lett. **13**, 60 (2021). https://doi.org/10.1007/s40820-020-00581-4

22. F. Dong, M. Wu, Z. Chen, X. Liu, G. Zhang et al., Atomically dispersed transition metal-nitrogen-carbon bifunctional oxygen electrocatalysts for zinc-air batteries: recent advances and future perspectives. Nano-Micro Lett. **14**, 36 (2021). https://doi.org/10.1007/s40820-021-00768-3

23. Y. Niu, X. Teng, S. Gong, M. Xu, S.G. Sun et al., Engineering two-phase bifunctional oxygen electrocatalysts with tunable and synergetic components for flexible Zn-air batteries. Nano-Micro Lett. **13**, 126 (2021). https://doi.org/10.1007/s40820-021-00650-2

24. Y. Zhang, F. Wan, S. Huang, S. Wang, Z. Niu et al., A chemically self-charging aqueous zinc-ion battery. Nat. Commun. **11**, 2199 (2020). https://doi.org/10.1038/s41467-020-16039-5

25. L. Yan, Y. Zhang, Z. Ni, Y. Zhang, J. Xu et al., Chemically self-charging aqueous zinc-organic battery. J. Am. Chem. Soc. **143**(37), 15369–15377 (2021). https://doi.org/10.1021/jacs.1c06936

26. W. Li, C. Han, Q. Gu, S.L. Chou, J.Z. Wang et al., Electron delocalization and dissolution-restraint in vanadium oxide superlattices to boost electrochemical performance of aqueous zinc-ion batteries. Adv. Energy Mater. **10**(48), 2001852 (2020). https://doi.org/10.1002/aenm.202001852

27. S. Liu, H. Zhu, B. Zhang, G. Li, H. Zhu et al., Tuning the kinetics of zinc-ion insertion/extraction in V_2O_5 by in situ polyaniline intercalation enables improved aqueous zinc-ion storage performance. Adv. Mater. **32**(26), e2001113 (2020). https://doi.org/10.1002/adma.202001113

28. J. Huang, Z. Wang, M. Hou, X. Dong, Y. Liu et al., Polyaniline-intercalated manganese dioxide nanolayers as a high-performance cathode material for an aqueous zinc-ion battery. Nat. Commun. **9**, 2906 (2018). https://doi.org/10.1038/s41467-018-04949-4

29. X. Ma, X. Cao, M. Yao, L. Shan, X. Shi et al., Organic-inorganic hybrid cathode with dual energy-storage mechanism for ultrahigh-rate and ultralong-life aqueous zinc-ion batteries. Adv. Mater. **34**(6), e2105452 (2022). https://doi.org/10.1002/adma.202105452

30. Z. Yao, Q. Wu, K. Chen, J. Liu, C. Li, Shallow-layer pillaring of a conductive polymer in monolithic grains to drive superior zinc storage via a cascading effect. Energy Environ. Sci. **13**(9), 3149–3163 (2020). https://doi.org/10.1039/d0ee01531h

31. D. Bin, W. Huo, Y. Yuan, J. Huang, Y. Liu et al., Organic-inorganic-induced polymer intercalation into layered composites for aqueous zinc-ion battery. Chem **6**(4), 968–984 (2020). https://doi.org/10.1016/j.chempr.2020.02.001

32. W. Bi, G. Gao, G. Wu, M. Atif, M.S. AlSalhi et al., Sodium vanadate/PEDOT nanocables rich with oxygen vacancies for high energy conversion efficiency zinc ion batteries. Energy Storage Mater. **40**, 209–218 (2021). https://doi.org/10.1016/j.ensm.2021.05.003

33. Z. Zhang, B. Xi, X. Wang, X. Ma, W. Chen et al., Oxygen defects engineering of $VO_2 \cdot xH_2O$ nanosheets via in situ polypyrrole polymerization for efficient aqueous zinc ion storage. Adv. Funct. Mater. **31**(34), 2103070 (2021). https://doi.org/10.1002/adfm.202103070

34. L. Hu, Z. Wu, C. Lu, F. Ye, Q. Liu et al., Principles of interlayer-spacing regulation of layered vanadium phosphates for superior zinc-ion batteries. Energy Environ. Sci. **14**(7), 4095–4106 (2021). https://doi.org/10.1039/d1ee01158h

35. S. Li, Y. Liu, X. Zhao, K. Cui, Q. Shen et al., Molecular engineering on MoS_2 enables large interlayers and unlocked basal planes for high-performance aqueous Zn-ion storage. Angew. Chem. Int. Ed. **60**(37), 20286–20293 (2021). https://doi.org/10.1002/anie.202108317

36. H. Liang, Z. Cao, F. Ming, W. Zhang, D.H. Anjum et al., Aqueous zinc-ion storage in MoS_2 by tuning the intercalation energy. Nano Lett. **19**(5), 3199–3206 (2019). https://doi.org/10.1021/acs.nanolett.9b00697

37. J. Liu, P. Xu, J. Liang, H. Liu, W. Peng et al., Boosting aqueous zinc-ion storage in MoS_2 via controllable phase. Chem. Eng. J. **389**, 124405 (2020). https://doi.org/10.1016/j.cej.2020.124405

38. H. Liu, J.G. Wang, W. Hua, Z. You, Z. Hou et al., Boosting zinc-ion intercalation in hydrated MoS_2 nanosheets toward substantially improved performance. Energy Storage Mater. **35**, 731–738 (2021). https://doi.org/10.1016/j.ensm.2020.12.010

39. W. Xu, C. Sun, K. Zhao, X. Cheng, S. Rawal et al., Defect engineering activating (boosting) zinc storage capacity of MoS_2. Energy Storage Mater. **16**, 527–534 (2019). https://doi.org/10.1016/j.ensm.2018.09.009

40. H. Li, Q. Yang, F. Mo, G. Liang, Z. Liu et al., MoS_2 nanosheets with expanded interlayer spacing for rechargeable aqueous Zn-ion batteries. Energy Storage Mater. **19**, 94–101 (2019). https://doi.org/10.1016/j.ensm.2018.10.005

41. S. Li, Y. Liu, X. Zhao, Q. Shen, W. Zhao et al., Sandwich-like heterostructures of MoS_2/graphene with enlarged interlayer spacing and enhanced hydrophilicity as high-performance cathodes for aqueous zinc-ion batteries. Adv. Mater. **33**(12), e2007480 (2021). https://doi.org/10.1002/adma.202007480

42. C. Li, C. Liu, Y. Wang, Y. Lu, L. Zhu et al., Drastically-enlarged interlayer-spacing MoS_2 nanocages by inserted carbon motifs as high performance cathodes for aqueous zinc-ion batteries. Energy Storage Mater. **49**, 144–152 (2022). https://doi.org/10.1016/j.ensm.2022.03.048

43. J. Jiang, Z. Chen, Y. Hu, Y. Xiang, L. Zhang et al., Flexophotovoltaic effect in MoS_2. Nat. Nanotechnol. **16**(8), 894 (2021). https://doi.org/10.1038/s41565-021-00919-y

44. X. Zhang, Q. Liao, S. Liu, Z. Kang, Z. Zhang et al., Poly(4-styrenesulfonate)-induced sulfur vacancy self-healing strategy for monolayer MoS_2 homojunction photodiode. Nat. Commun. **8**, 15881 (2017). https://doi.org/10.1038/ncomms15881

45. W. Zhang, Y. Liu, X. Pei, Z. Yuan, Y. Zhang et al., Stretchable MoS_2 artificial photoreceptors for e-skin. Adv. Funct. Mater. **32**(10), 2107524 (2022). https://doi.org/10.1002/adfm.202107524

46. J. Shi, S. Wang, X. Chen, Z. Chen, X. Du et al., An ultrahigh energy density quasi-solid-state zinc ion microbattery with excellent flexibility and thermostability. Adv. Energy Mater. **9**(37), 1901957 (2019). https://doi.org/10.1002/aenm.201901957

47. J. Shi, S. Wang, Q. Wang, X. Chen, X. Du et al., A new flexible zinc-ion capacitor based on δ-MnO_2@carbon cloth battery-type cathode and MXene@cotton cloth capacitor-type anode. J. Power Sour. **446**, 227345 (2020). https://doi.org/10.1016/j.jpowsour.2019.227345

48. F. Cui, D. Wang, F. Hu, X. Yu, C. Guan et al., Deficiency and surface engineering boosting electronic and ionic kinetics in $NH_4V_4O_{10}$ for high-performance aqueous zinc-ion battery. Energy Storage Mater. **44**, 197–205 (2022). https://doi.org/10.1016/j.ensm.2021.10.001

49. J. Shi, Y. Hou, Z. Liu, Y. Zheng, L. Wen et al., The high-performance MoO_{3-x}/MXene cathodes for zinc-ion batteries based on oxygen vacancies and electrolyte engineering. Nano

Energy **91**, 106651 (2022). https://doi.org/10.1016/j.nanoen.2021.106651

50. P. Zheng, T. Li, K. Chi, C. Xiao, J. Fan et al., DFT insights into the formation of sulfur vacancies over corner/edge site of Co/Ni-promoted MoS_2 and WS_2 under the hydrodesulfurization conditions. Appl. Catal. B Environ. **257**, 117937 (2019). https://doi.org/10.1016/j.apcatb.2019.117937

51. Y. Tian, L. Xu, M. Li, D. Yuan, X. Liu et al., Interface engineering of CoS/CoO@N-doped graphene nanocomposite for high-performance rechargeable Zn-air batteries. Nano-Micro Lett. **13**, 3 (2020). https://doi.org/10.1007/s40820-020-00526-x

52. N.K. Wagh, S.S. Shinde, C.H. Lee, S.H. Kim, D.H. Kim et al., Supramolecular polymer intertwined free-standing bifunctional membrane catalysts for all-temperature flexible Zn-air batteries. Nano-Micro Lett. **14**, 190 (2022). https://doi.org/10.1007/s40820-022-00927-0

53. W.S.V. Lee, T. Xiong, X. Wang, J. Xue, Unraveling MoS_2 and transition metal dichalcogenides as functional zinc-ion battery cathode: a perspective. Small Methods **5**(1), e2000815 (2021). https://doi.org/10.1002/smtd.202000815

54. H. Zhang, W. Wu, Q. Liu, F. Yang, X. Shi et al., Interlayer engineering of alpha-MoO_3 modulates selective hydronium intercalation in neutral aqueous electrolyte. Angew. Chem. Int. Ed. **60**(2), 896–903 (2021). https://doi.org/10.1002/anie.202010073

55. Y. Xue, Y. Guo, Q. Zhang, Z. Xie, J. Wei et al., MOF-derived Co and Fe species loaded on N-doped carbon networks as efficient oxygen electrocatalysts for Zn-air batteries. Nano-Micro Lett. **14**, 162 (2022). https://doi.org/10.1007/s40820-022-00890-w

56. Y. Zhu, K. Yue, C. Xia, S. Zaman, H. Yang et al., Recent advances on MOF derivatives for non-noble metal oxygen electrocatalysts in zinc-air batteries. Nano-Micro Lett. **13**, 137 (2021). https://doi.org/10.1007/s40820-021-00669-5

57. T. Jain, B.C. Rasera, R.J.S. Guerrero, M.S.H. Boutilier, S.C. O'Hern et al., Heterogeneous sub-continuum ionic transport in statistically isolated graphene nanopores. Nat. Nanotechnol. **10**(12), 1053 (2015). https://doi.org/10.1038/nnano.2015.222

58. W. Xin, J. Fu, Y. Qian, L. Fu, X.Y. Kong et al., Biomimetic KcsA channels with ultra-selective K^+ transport for monovalent ion sieving. Nat. Commun. **13**, 1701 (2022). https://doi.org/10.1038/s41467-022-29382-6